AIP | The Journal of Chemical Physics

Pulse-shaping assisted multidimensional coherent electronic spectroscopy

Yuseff Rodriguez, Franziska Frei, Andrea Cannizzo, and Thomas Feurer

Citation: The Journal of Chemical Physics **142**, 212451 (2015); doi: 10.1063/1.4921793
View online: http://dx.doi.org/10.1063/1.4921793
View Table of Contents: http://scitation.aip.org/content/aip/journal/jcp/142/21?ver=pdfcov
Published by the AIP Publishing

Pulse-shaping assisted multidimensional coherent electronic spectroscopy

Yuseff Rodriguez, Franziska Frei,[a] Andrea Cannizzo,[b] and Thomas Feurer
Institute of Applied Physics, University of Bern, Sidlerstasse 5, CH-3012 Bern, Switzerland

(Received 27 February 2015; accepted 14 May 2015; published online 2 June 2015)

Understanding nuclear and electronic dynamics of molecular systems has advanced considerably by probing their nonlinear responses with a suitable sequence of pulses. Moreover, the ability to control crucial parameters of the excitation pulses, such as duration, sequence, frequency, polarization, slowly varying envelope, or carrier phase, has led to a variety of advanced time-resolved spectroscopic methodologies. Recently, two-dimensional electronic spectroscopy with ultrashort pulses has become a more and more popular tool since it allows to obtain information on energy and coherence transfer phenomena, line broadening mechanisms, or the presence of quantum coherences in molecular complexes. Here, we present a high fidelity two-dimensional electronic spectroscopy setup designed for molecular systems in solution. It incorporates the versatility of pulse-shaping methods to achieve full control on the amplitude and phase of the individual exciting and probing pulses. Selective and precise amplitude- and phase-modulation is shown and applied to investigate electronic dynamics in several reference molecular systems. [http://dx.doi.org/10.1063/1.4921793]

I. INTRODUCTION

Since femtosecond pulse shaping with spatial light modulators (SLMs) was fully developed in the 1990s,[1] it has found versatile applications in many different fields. Nowadays, pulse shaping is used for optical pulse compression, coherent control, in nonlinear spectroscopy, or bio-imaging applications.[1–5] The unique capability of pulse shaping methodologies to provide phase stable pulses is well accepted and several schemes have been proposed to implement four-wave mixing (FWM) spectroscopies based on pulse shaping.[6,7] A further unique advantage of such setups is the capability to enhance specific signal contributions and to suppress background due to scattering by phase-cycling the interacting pulses. This was successfully proven first in a collinear geometry.[8] While non-collinear FWM setups exhibit an inherently much better background rejection, shaping of the different interacting pulses becomes more complex. Recently, non-collinear FWM spectrometers have been implemented where only the pump pulse is replaced by a pair of pulses generated via pulse shaping.[6] This approach provides a very robust setup for multidimensional spectroscopy and is relatively easy to implement. However, two aspects limit the signal-to-noise ratio of such an approach: (i) when compared to fully collinear schemes the extent of background rejection with phase-cycling is rather limited because the third pulse, i.e., the probe, is not phase-locked to the first two pulses; (ii) the third pulse plays also the role of local oscillator (LO) but, unlike in most standard non-collinear schemes, its intensity and delay with respect to the signal cannot be optimized to the best conditions for interferometric detection.

To fully benefit from both, the non-collinear geometry and pulse generation entirely based on pulse shaping, a non-collinear FWM setup was implemented where all the four pulses can be shaped by the same pulse-shaper employing a two-dimensional (2D) liquid crystal SLM.[9–12] That is, on the one hand, all the pulses are inherently phase-locked, and on the other hand, each pulse can be independently tailored. This configuration nicely proved the principle, the enhanced versatility and was applied in several experiments. However, it shows practical limitations that prevented so far such approach to become a state-of-the-art technique in molecular spectroscopy. First, the energy throughput is rather low (<1%). To achieve fluences suitable for molecular spectroscopy (typically 100 (nJ/pulse)/beam, that is >300 nJ/pulse at the sample position) requires 0.5–1 mJ laser sources which, with current laser technology, can be generated only at a few kHz repetition rates. Such low repetition rates impede background free experiments, e.g., non-collinear FWM, which benefits from averaging over a large number of pulses. Second, amplitude pulse shaping unavoidable decreases the overall intensity further and therefore can often not be applied. Third, the reported phase stability of $\lambda/67$ at $\lambda = 800$ nm, which is sufficient for experiments in the near-infrared (NIR), is already borderline in the visible range, not to mention the UV region.

Motivated by the potential of such an experimental technique in advancing the scientific understanding of molecular dynamics, we implemented a pulse-shaping assisted non-collinear FWM setup conceived to operate at repetition rates in excess of 100 kHz, at fluences as low as 1–10 μJ/pulse, and suitable for the visible spectral region. This implied an improvement of the energy throughput by one order of magnitude and of the phase-stability by at least a factor of 2. Such a setup allows carrying out coherent electronic spectroscopy on molecular systems with a full and independent control of the

[a]Current address: Paul Scherrer Institut, 5232 Villigen PSI - Switzerland.
[b]Electronic mail: andrea.cannizzo@iap.unibe.ch

temporal properties of each of the four pulses. In particular, time scans of picoseconds with 150 as precision are possible with no movable mechanical parts in the setup and the four pulses can be independently compressed or shaped at the sample position.

In this contribution, we first report on the main characteristics of the experimental setup. To prove its performances and unique versatility, we show several examples from different molecular systems and an outlook on the experimental methodologies possible only with this setup and not with conventional implementations. The setup was already successfully used to investigate several molecular systems and in particular metal complexes in solution.[13] Here, we focus on two reference molecular systems: pure diiodomethane and the dye IR-144 in methanol. Both molecules were already investigated with heterodyne-detected transient grating (TG)[14] and photon echo (PE)[15–19] techniques, respectively; therefore, they are ideal to prove and establish our advanced nonlinear spectroscopy methodologies.

II. EXPERIMENTAL IMPLEMENTATION

Independent amplitude and phase control is the main characteristic of our experimental configuration, conceived for inherently phase-stabilized multidimensional spectroscopy with versatile pulse shaping capabilities.[10,11] The FWM setup is illustrated in Fig. 1(a). To generate four stable pulses in the desired boxcar geometry, the incoming collimated output of an amplified Ti:sapphire laser (center wavelength of 805 nm, FWHM 35 nm, 250 kHz repetition rate), model Rega 9050 (Coherent, Inc.) is first focused (f_1 = 400 mm) onto a commercial 2D phase mask (Laser Components, GmbH). This focus is thereon imaged (f_2 = 200 mm, f_3 = 1000 mm) to the pickoff mirror plane. The following spherical lens (f_4 = 500 mm) images the pickoff plane back to itself via the modulator. The grating (600 lines/mm) in the 4f-compressor disperses the four incoming pulses in the horizontal direction, and a cylindrical lens (f_c = 200 mm) focuses and collimates each spectral component at the SLM (Hamamatsu, model X10468-02) with 792 × 600 nematic liquid crystal pixels each 20 × 20 μm in size. To distribute the four spectra equidistantly on the vertical modulator dimension, the boxcar geometry formed by the four beams is tilted by 26.6°. In order to modulate the amplitude and phase of each spectral component, a blazed phase grating pattern is transferred to the modulator to diffract the first order downwards onto the pickup mirror which sends the diffracted beam to the experiment. The two following lenses (f_5 = 300 mm and f_6 = 100 mm) are selected so that the focal spot size is roughly 100 μm $1/e^2$. The overall throughput efficiency between the incoming beam and the experimental plane in Fig. 1(a) was measured to be 14%. A maximum fluence of 150 (nJ/pulse)/beam was achievable but a typical value of 10–30 (nJ/pulse)/beam was used, if not differently specified.

This configuration has several advantages: (i) each pulse can be independently addressed on the SLM, (ii) the amplitude and phase of each spectral component can be arbitrarily controlled by modulating the amplitude of the phase grating and by vertically shifting contiguous pixel columns by fraction of the grating period, respectively, (iii) only shaped light is

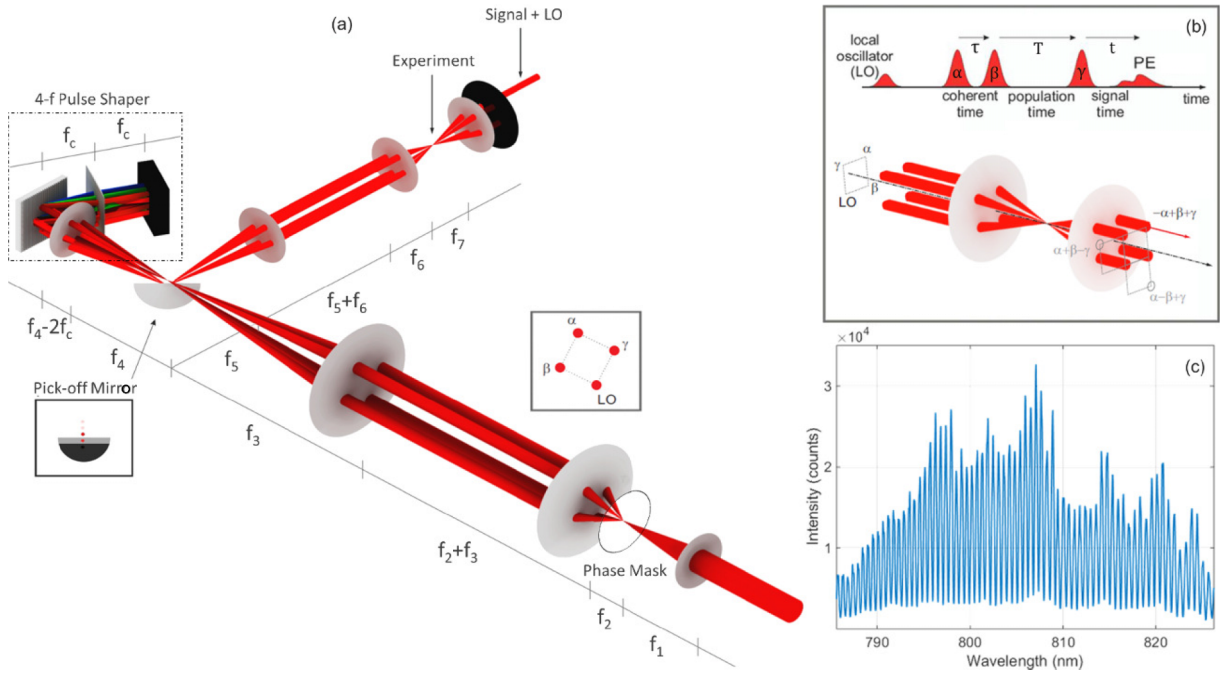

FIG. 1. Automated, pulse-shaping-assisted, coherent four wave mixing setup. (a) Layout of the setup: four phase-stable pulses are generated by focusing the incoming beam (λ = 805 nm, $\Delta\lambda$ = 35 nm, repetition rate 250 kHz, pulse energy 1-2 μJ) on a 2D phase mask. The latter is turned by 26.6° around the beams propagation direction, and the re-collimated four beams propagate in a tilted boxcar geometry (see inset). In such a way, the four beams are equally vertically displaced on the Fourier plane of the shaper and can be individually addressed on the SLM. The independently shaped pulses are collected by a pickup mirror and sent to the sample. A variable neutral density filter (not shown) is inserted in the path of the LO between the first two lenses. (b) Time sequence, geometry, and notation of the pulses at the sample position. (c) A representative experimental interferogram of the photon echo (PE) signal and LO (and undesired scattering from the other beams; see text for details) detected in our setup on a solution of IR-144 in methanol at $\tau = T = 0$ fs and the LO delayed by 3.7 ps.

collected, while the unshaped light, pulse replicas and most of the scattering is reflected back to the zeroth diffraction order, (iv) a remarkable throughput is achieved when compared to similar schemes[9–11] because the four phase-stable beams are generated with a phase mask and the shaped beams are picked off by a mirror being spatially separated from the incoming ones, (v) since the setup is conceived as a sequence of image planes with long focal distances (therefore mm to cm confocal regions), it is virtually insensitive to pointing fluctuations of the main laser beam.

Mathematically, the effect of the SLM on the incoming electromagnetic field $E_0(\omega)$ of each pulse is described in terms of a complex transfer function (TF) $M(\omega)$ which modulates both the amplitude and phase of $E_0(\omega)$,

$$E(\omega) = E_0(\omega)\, M(\omega) = E_0(\omega)\, A(\omega)\, e^{i\Phi(\omega)}, \qquad (1)$$

where $E(\omega)$ is the shaped field, while $A(\omega)$ and $\Phi(\omega)$ are the amplitude and phase of the TF, spanning from 0 to 1 and $-\pi$ to π, respectively. The setup is designed according to an imaging geometry to minimize distortions arising from space-time coupling (0.625 mm/ps),[20] as well as the frequency dependent diffraction from the phase mask. Fig. 1(b) shows the pulse sequence at the experimental plane and the given phase matching conditions for the boxcar geometry. After the experimental plane, the phase matched signal ($-\alpha + \beta + \gamma$ for the rephasing pulse sequence) co-propagates along with the LO. Two diaphragms block the three beams before the signal field is spatially filtered with a 100 μm pinhole for further elimination of zero-order contributions from the pickoff mirror. Thereafter, the pinhole is imaged onto the entrance slit of the spectrometer (Andor Shamrock SR-500, equipped with a Newton EMCCD), where the heterodyned signal is detected. To set an optimal heterodyne detection, it is necessary (i) to decrease the LO intensity to be comparable or at most two orders of magnitude stronger than the signal and (ii) to be delayed by several ps with respect to the signal and the third pulse to generate a strong interference. Both conditions are achieved by inserting a variable neutral density filter with a 2 mm thickness in the LO path (higher order dispersion terms due to the propagation through the filter can be compensated by the shaper). In Fig. 1(c) is shown a typical spectral interferogram for τ, T set to zero, and a LO delayed by 3.7 ps. This value is chosen to have an high number of well resolved fringes as observed in Fig. 1(c).

To assure a correct phase and amplitude modulation on the SLM, an accurate pixel to wavelength calibration is indispensable. The wavelength of each SLM pixel-column for each horizontal beam allocation is calibrated by applying an amplitude window modulation (1 at the given pixel column with one to few pixels width, 0 elsewhere) and detecting the corresponding diffracted spectral component with a spectrometer. Thereafter, the window position is shifted horizontally by one pixel, and the spectral measurement is repeated. This procedure provides a full experimental pixel to wavelength calibration curve, which can also be fitted to a grating equation.

For FWM experiments, even in cases when shaped pulses are used, it is essential to determine first the phase corrections that are required to obtain transform-limited pulses at the sample position. Phase distortions may arise from the main laser pulse or the different optical paths of the beams. The SLM can be programmed to realize such spectral phase corrections. For this purpose, the four beams can be directed to a 20 μm beta barium borate (BBO) crystal for an *in situ* pulse characterization (Fig. 2(a)). After passing through a bandpass filter centered at 400 nm (3 mm thick BG39 filter), the spatially resolved second harmonic pattern is detected by a camera. When all four pulses overlap in time nine SHG spots appear. The four corner spots are due to second harmonic generation of the individual pulses. The median spots originate from frequency mixing of beams at the neighboring corners; however, the median spots involving the LO (the spot on the bottom right in the inset) are normally absent since the LO is delayed by 3.7 ps. The central spot is due to the interaction between the pulses from the corner spots along the two diagonals. For phase correction, we integrate the intensities of the four corner spots individually. For each of the four pulses, we scan the second and third order phases until their second harmonic intensity is maximized and close to transform limited pulse is reached.

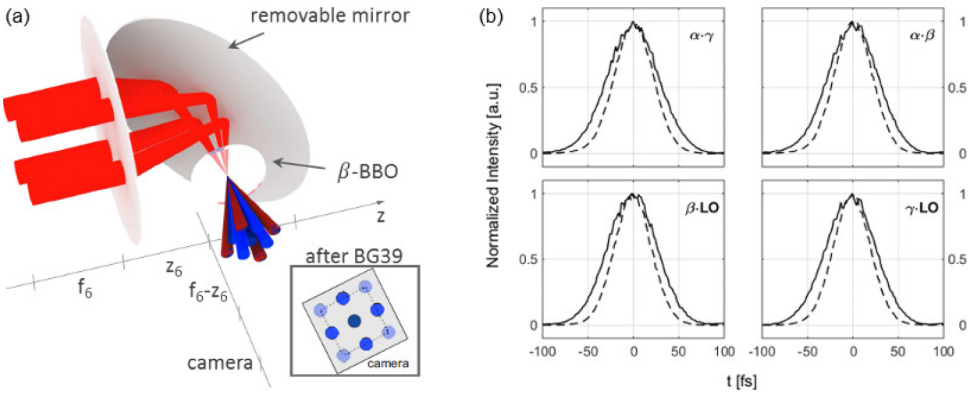

FIG. 2. Phase compensation measurements. (a) The four beams at the sample position are focused on a 20 μm thick beta barium borate (BBO) crystal to generate a second harmonic pattern detected with a camera. The beams overlapping in time are not only producing second harmonics in the four corners but also the cross correlation signals can be observed. This leads to the spot pattern shown in the inset. (b) Normalized second order cross correlation intensities measured from the second harmonic generation process due to the interaction of two continuous pulse pairs at the BBO (each scan is labeled with the name of the correlated pulses according to the notation from Fig. 1). Solid and dashed lines show scans with normal and broadened band pulses, respectively (see Sec. III A for details).

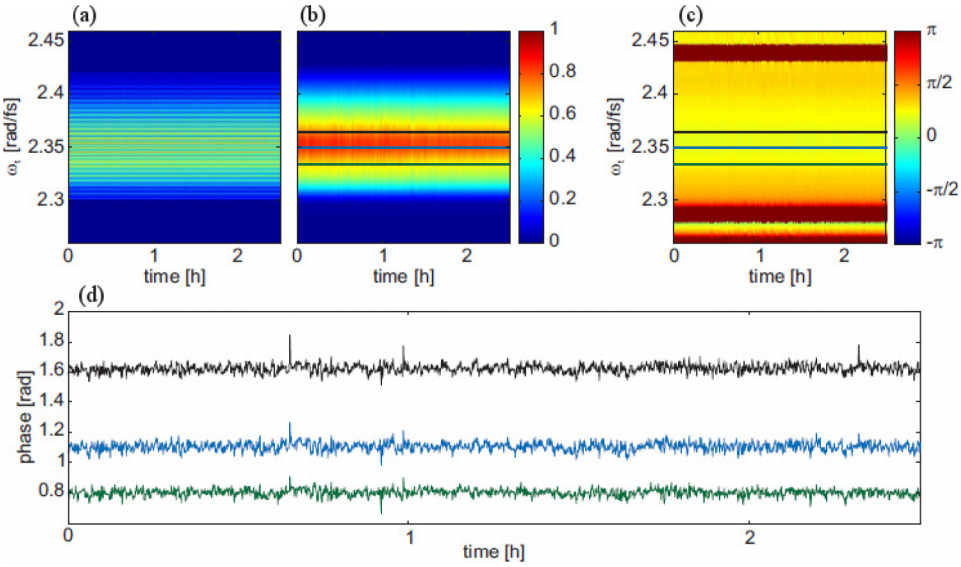

FIG. 3. Phase stability analyzed over a period of 2.5 h, where the signal intensity was approximately constant. The spectral interference fringes of the heterodyned signal for $T = \tau = 0$ fs are shown in (a). After isolating the heterodyned signal field in the time domain, the absolute value of the spectral field of interest is shown in (b). The corresponding spectral phase is depicted in (c). For three different detection frequencies indicated in (b) and (c), the temporal traces are displayed in (d). For a better visibility, an offset is added per trace.

The time synchronization to define time zero is accomplished by scanning the first order spectral phase coefficients of the two pulses α and β relative to the pulse γ until the intensity of the respective median spots is maximized (other scanning schemes where another pulse is taken as a reference are equivalent). The outcome of this procedure is a TF for each pulse with unity amplitude which compensates for all dispersion terms considered

$$M_{FL}(\omega) = \mathrm{e}^{\mathrm{i}(\Phi(\omega)-\omega t_i)}, \tag{2}$$

where t_i is the time delay with respect to the reference pulse. In other words by setting $t_\alpha = 0$ ($t_\beta = 0$), the pulse α (β) is time overlapped with the pulse γ. Fig. 2(b) shows the characteristic cross correlation scans between two different pulse pairs, including also the LO, which for most of the cases is delayed in order to perform heterodyne detections.

Since heterodyne detection is phase sensitive, any unbalanced sub-wavelength change in the optical path of one of the four beams will induce a shift of the detected spectral interference fringes. In particular, unbalanced mechanical instabilities on the order of $\lambda/10$ or more of one of the four beams will end up with a severe degradation of the interference pattern with the impossibility to retrieve any PE signal. By design, our setup should not be affected by this issue because all the beams follow a common path passing through or being reflected by the same optical elements. To verify the phase stability, the heterodyned signal for $T = \tau = 0$ fs (LO delayed by 3.7 ps) was measured over 2.5 h in steps of 5 s. The recorded spectral interference fringes shown in Fig. 3(a) were Fourier transformed along the detection axis to the temporal domain where the heterodyned signal was isolated around the delay time of the local oscillator. As shown in Fig. 3(b), the absolute value of the inverse Fourier transformed relevant field is approximately constant over the time period under consideration. For three detection frequencies, traces of the corresponding phase (Fig. 3(c)) are shown in Fig. 3(d). To improve the visibility, an offset is added per trace. Over 2.5 h, the phase was stable within 0.027 rad which corresponds to $\lambda/233$ or $\Delta = 3.5$ nm.

A common problem even with non-collinear FWM setups is that scattering from the three interacting pulses does contaminate the detected signal, which is typically 3–4 orders of magnitude smaller than the incoming pulses and thus comparable or even smaller than the scattering contributions. This makes a background rejection procedure necessary to extract such small signals. In the presence of scattering, the detected intensity is given by

$$I_{det}(\phi_{0,\alpha},\phi_{0,\beta},\phi_{0,\gamma},\phi_{0,LO}) \propto \left|E_{LO}\mathrm{e}^{\mathrm{i}\phi_{0,LO}} + E_s\mathrm{e}^{\mathrm{i}\phi_{0,s}} + \epsilon\left(E_\alpha\mathrm{e}^{\mathrm{i}\phi_{0,\alpha}} + E_\beta\mathrm{e}^{\mathrm{i}\phi_{0,\beta}} + E_\gamma\mathrm{e}^{\mathrm{i}\phi_{0,\gamma}}\right)\right|^2. \tag{3}$$

where ϵ denotes the fraction of the pulse amplitude which is scattered. For simplicity, ϵ will be set to one for further calculations. According to the phase matching condition, the absolute phase of the signal is given by $\phi_{0,s} = -\phi_{0,\alpha} + \phi_{0,\beta} + \phi_{0,\gamma}$. The measured intensity thus contains ten cross terms

$$\begin{aligned} I_{det}(\phi_{0,\alpha},\phi_{0,\beta},\phi_{0,\gamma},\phi_{0,LO}) \propto\ & |E_{LO}|^2 + |E_s|^2 + |E_\alpha|^2 + |E_\beta|^2 + |E_\gamma|^2 + 2\big[E_{LO}E_s^*\cos(\phi_{0,LO}-\phi_{0,s}) + E_{LO}E_\alpha^*\cos(\phi_{0,LO}-\phi_{0,\alpha}) \\ & + E_{LO}E_\beta^*\cos(\phi_{0,LO}-\phi_{0,\beta}) + E_{LO}E_\gamma^*\cos(\phi_{0,LO}-\phi_{0,\gamma}) + E_sE_\alpha^*\cos(\phi_{0,s}-\phi_{0,\alpha}) + E_sE_\beta^*\cos(\phi_{0,LO}-\phi_{0,\beta}) \\ & + E_sE_\gamma^*\cos(\phi_{0,s}-\phi_{0,\gamma}) + E_\alpha E_\beta^*\cos(\phi_{0,\alpha}-\phi_{0,\beta}) + E_\alpha E_\gamma^*\cos(\phi_{0,\alpha}-\phi_{0,\gamma}) + E_\beta E_\gamma^*\cos(\phi_{0,\beta}-\phi_{0,\gamma})\big]. \end{aligned} \tag{4}$$

A common approach in conventional non-collinear setups is to cyclically block the different beams to isolate the different scattering contributions and subtract them from the measurement with all beams on. From Eq. (4), it can be easily derived that at least four measurements are necessary to isolate the relevant term $E_{LO}E_s^*\cos(\phi_{0,LO}-\phi_{0,s})$ (for instance, all the beams on, the γ beam off only, the α and β pulses off, and the LO beam off only). However, this method has two crucial

TABLE I. Phase cycling scheme.

No.	α	β	γ	LO
M1	0	0	0	0
M2	0	π	0	0
M3	π	π	0	0
M4	π	0	0	0
M5	0	0	0	π
M6	0	π	0	π
M7	π	π	0	π
M8	π	0	0	π

limitations: (i) the four experiments are not carried out under identical experimental conditions because in each measurements a different amount of energy per pulse sequence is delivered to the sample, and changes in transient incoherent effects (e.g., thermal effect or transient absorption) could generate artifacts, (ii) only one measurement contains the signal; thus, the background subtraction will decrease the signal-to-noise ratio, and the experimental duty cycle is 25% only.

With our setup, a phase-cycling rejection approach can be adopted. Indeed since the scattering cross terms have a different dependence on the absolute phase compared to the desired first term, $E_{LO}E_s^*\cos(\phi_{0,LO}-\phi_{0,s})$ can be isolated by a phase cycling procedure with eight measurements (M_i). The eight phase combinations needed are listed in Table I. By adding them according to

$$((M2-M1)-(M3-M4))-((M6-M5)-(M7-M8)), \tag{5}$$

the term $2\cdot 8E_{LO}E_s^*\cos(\phi_{0,LO}-\phi_{0,s})$ can be isolated. Through this phase cycling procedure, not only the scattering terms are suppressed but also the signal term is enhanced by a factor of eight with respect to a single measurement. Each data set contains the signal contribution and the total duty cycle is still 100%. In addition, the sample spot is excited always by all four beams with the same intensity, and transient incoherent effects can be considered to be similar for all measurements.

As an example, the eight individual scans for a photon echo measurement of the dye IR-144 in methanol with $T = 400$ fs are shown in Fig. 4. The LO is stronger than the signal, nevertheless spectral fringes should only be observable, if the signal is interfering with the LO around $\tau = 0$ fs. The separate measurements in Fig. 4 show a signal contaminated with strong scattering though. To suppress scattering as well as to eliminate the contribution arising from the local oscillator only, in Fig. 5 the eight measurements are combined according to Eq. (5). Now, the signal is clearly observable; the color map is normalized to the same value as in Fig. 4. Also, in the phase-cycled measurement (Fig. 5), the intensity is localized around $\tau = 0$ fs which indicates that the term $E_{LO}E_s^*\cos(\phi_{L0}-\phi_s)$ has been significantly enhanced with respect to the scattering terms.

Phase cycling can also be used to enhance scattering from a desired beam. In particular to enhance the interferogram originating from a given cross term $E_{LO}E_i^*$ ($i=\alpha,\beta,\gamma$). This possibility can be used to perform an intrinsic time delay calibration for each beam with respect to the LO. In this way, we estimated time resolution and repeatability uncertainty of our setup to be better than 150 as.

III. SHAPER-ASSISTED CONCEPTS FOR NONLINEAR OPTICAL SPECTROSCOPY

In coherent two-dimensional electronic spectroscopy (2D-ES), the fundamental quantity of interest is the time-dependent, oscillatory molecular signal field $E_s^{(3)}(\tau,T,t)$, where τ and T represent the two time intervals between the three pulse-molecule interactions and t denotes the elapsed time after the third pulse and the beginning of the signal field emission (see Fig. 1(b)). Under perfect phase matching conditions, this signal field is proportional to the third order

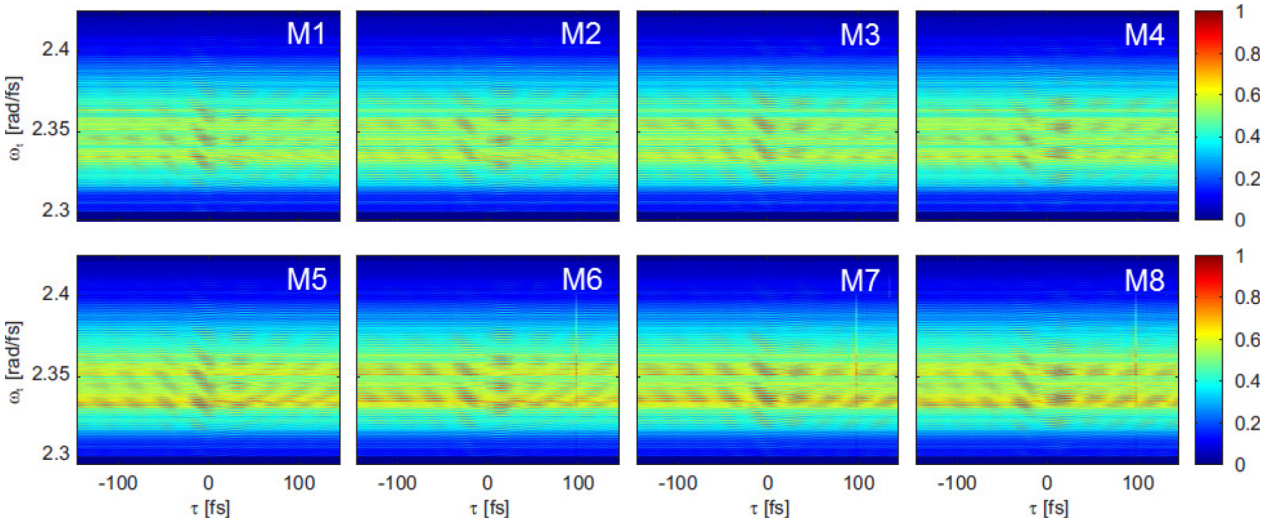

FIG. 4. Background suppression by phase-cycling: eight photon echo measurements on IR-144 in methanol at $T = 400$ fs phase-cycled according to Table I are shown. Color map is the same for all the plots. The background free photon echo signal is calculated combining these measurements according to Eq. (5) and it is shown in Fig. 5. All the 2D plots show an important scattering contribution, largely generated at the SLM surface (see Fig. 1(a), inset corresponding to 4-f pulse shaper). Since this field is phase-stable with the shaped pulses, it gives origin to the observed interference pattern. The vertical line observed at 100 fs in plots M6–M8 is an experimental artefact.

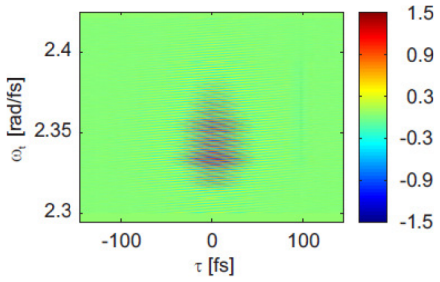

FIG. 5. Background free photon echo signal after combining the eight phase-cycled measurements shown in Fig. 4 according to Eq. (5). The color map is the same as in Fig. 4.

polarization $P^{(3)}(\tau,T,t)$ with signal wavevector architecture $\boldsymbol{k_I} = -\boldsymbol{k_\alpha} + \boldsymbol{k_\beta} + \boldsymbol{k_\gamma}$ (photon echo, rephasing pulse sequence) and is expressed as a convolution of the optical response function $R^{(3)}(\tau,T,t)$ and the electric fields $E_\alpha(\boldsymbol{k_\alpha},t)$, $E_\beta(\boldsymbol{k_\beta},t)$, and $E_\gamma(\boldsymbol{k_\gamma},t)$ of the laser pulses with wavevectors $\boldsymbol{k_\alpha}$, $\boldsymbol{k_\beta}$, and $\boldsymbol{k_\gamma}$, respectively,[21,22]

$$P^{(3)}(\boldsymbol{k}_I,\tau,T,t) = \iiint dt'dT'd\tau'\, R^{(3)}(t',T',\tau')E_\gamma(\boldsymbol{k}_\gamma,t-t') \times E_\beta(\boldsymbol{k}_\beta,t-t'-T'+T) \times E^*_\alpha(\boldsymbol{k}_\alpha,t-t'-T'+T-\tau'+\tau) \quad (6)$$

In a similar way, $\boldsymbol{k_{II}} = \boldsymbol{k_\alpha} - \boldsymbol{k_\beta} + \boldsymbol{k_\gamma}$ (optical free induction decay, non-rephasing pulse sequence) can be calculated as well. The first pulse $\boldsymbol{k_\alpha}$ creates a coherence between the ground and the excited electronic states. The second pulse $\boldsymbol{k_\beta}$ after time τ converts the freely evolving coherence into an electronic population (population grating) and/or a vibrational coherence in the ground or excited state, which relaxes via dephasing processes during the time interval T. Finally, the third pulse $\boldsymbol{k_\gamma}$ after time T interacts with the decaying population/coherence and creates a coherent macroscopic dipole/response whose super-radiance generates the signal along $\boldsymbol{k_I}$ or $\boldsymbol{k_{II}}$, depending on the order of the interactions.

Different detection schemes have been proposed and implemented[21] to measure $E_s^{(3)}(\tau,T,t)$ and to derive from it insights into the system under investigation. Among all methodologies, heterodyne Fourier transform (FT) methods have proven to be particularly powerful approaches. Here, the electromagnetic field $E_s^{(3)}(\tau,T,t)$ is mixed with an external known field (LO) to achieve an interferometric heterodyne detection able to fully characterize both the amplitude and phase of the signal $E_s^{(3)}(\tau,T,\omega_t)$. Usually this signal is then Fourier transformed with respect to τ to obtain a 2D frequency-frequency plot of the signal $E_s^{(3)}(\omega_\tau,T,\omega_t)$ at a given population time T. Because relevant to further discussion, we have to specifically mention the three pulse photon echo peak shift (PEPS) technique. In this case, the signal is simply detected with a homodyne, non-spectrally resolved detection (a photo-multiplier tube or a photodiode), and for each T, a scan as a function of τ is performed to find the value of τ which maximizes the signal (the so-called PEPS). The decay of PEPS versus T reports on the electronic and vibrational decoherence of the system.[21,23]

2D-ES has experienced great advances in recent years,[24–27] with an additional boost after the implementation of passive phase-stable schemes[28,29] which allow to push 2D-ES from NIR[30] towards visible[29,31] and UV[32–34] domains. While these schemes provide a phase-stability good enough for a FT heterodyne detection, they cannot deliver, at the sample position, pulses with identical phase and amplitude, because of unavoidable differences in the optical path lengths. This limitation becomes more and more critical when using very broadband visible (nowadays bandwidths as wide as 200 nm can be easily generated[35–37]) or sub-100 fs UV pulses.[36] Thus, achieving independent control on the phase and the amplitude of each pulse, while preserving the mutual phase stability, is highly desirable and will potentially pave the way to novel detection schemes. Our setup fulfills all of these requirements, which we demonstrate in the following through a few selected proof-of-principle experiments.

A. Enhanced time-resolution spectroscopy

In conventional setups, the shortest time resolution is imposed by the spectral bandwidth of the main laser source, provided that all the optical elements constituting the setup are linear and broadband. Of course to fully benefit from the source bandwidth, it is mandatory to control the pulse dispersion at the sample position, which is one of the uncommon capabilities of our setup (see Sec. II, specifically Eq. (2)). While this intrinsic limit cannot be overcome with setups based on standard components, we can operate in this enhanced time resolved (ETR) regime by applying a transfer function to the SLM to produce an artificial broadening of the input spectrum and therefore an improvement on the instrumental response function of the system beyond the intrinsic one,

$$E(\omega) = E_0(\omega)\, M_{FL}(\omega)\, M_{ETR}(\omega) \quad (7)$$

where $M_{ETR}(\omega)$ is a TF modulating amplitude only, i.e., $\Phi_{ETR}(\omega) = 0$. We intend to enhance the bandwidth while keeping pulses Fourier limited at the sample; therefore, $M_{ETR}(\omega)$ has to act only on the amplitude of the compressed pulses. A possible realization is shown in Fig. 6. In this case, we chose

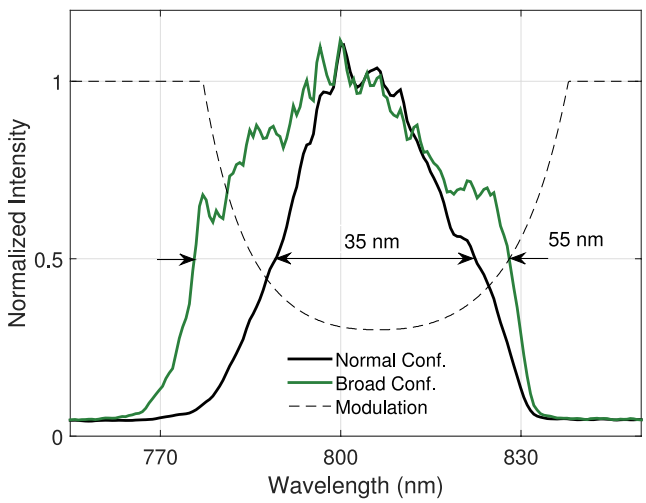

FIG. 6. Artificial broadening for enhanced time-resolution spectroscopy: TF applied to the SLM (dashed curve) in order to induce an spectrally broader pulse (green curve) compared to the input one (black curve).

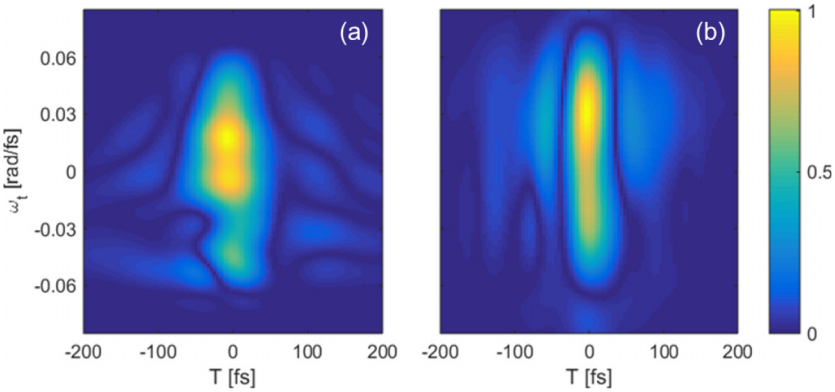

FIG. 7. TG-FROG traces measured for normal (a) and enhanced time-resolution (b) pulses, shown in Fig. 6. The corresponding second and third order autocorrelation values are reported in Table II.

$$M_{ETR}(\omega) = \min\left\{1, G\exp\left[\frac{n^2-1}{n^2}\,\frac{b(\omega-\omega_0)^2}{\Delta\omega_{in}^2}\right]^a\right\}, \quad (8)$$

where G, n, a, and b are parameters that can be adjusted (iteratively) for an optimal outcome. $\Delta\omega_{in}$ corresponds to the frequency FWHM of the input pulse and ω_0 is the central frequency. The width of the TF is parametrized via n with respect to $\Delta\omega_{in}$. The TF shown in Fig. 6 corresponds to $n = 2$, $G = 0.3$, $a = 1.2$, and $b = 2.36$.

Besides increasing the temporal resolution beyond that given by the laser system at hand, it is also noteworthy that a broader detection can potentially access more resonances of the investigated physical system. Fig. 7 shows TG frequency resolved optical gating (TG-FROG) traces measured for these two configurations, while the corresponding second and third order autocorrelation values are reported in Table II. We find a 27 % shortening of the third order autocorrelation trace which is the relevant number for FWM spectroscopy and should approximately coincide with the improvement in FWM time resolution. The possible extent of artificial broadening is limited only by the loss in power down to an intensity still enough to carry out the experiment. In our case, we worked with 10% of the initial power. Typically for experiments with NC pulses, fluences of ~20 (nJ/pulse)/beam for the three interacting beams and ~2 (nJ/pulse)/beam for the LO in 100 μm spots are used. In case of ETR pulses, typical fluences are ~2–5 (nJ/pulse)/beam and 0.5–1 (nJ/pulse)/beam in 100 μm spots for the main and the LO pulses, respectively. It has to be noted that any comparison between the input and output spectra has to be done after normalization, as it is the case in Fig. 6.

TABLE II. Calculated and measured time lengths (FWHM) for normal (NC) and broad (BC) configurations. Second and third order autocorrelation values are reported for both cases. The experimental values are estimated from cross correlation and TG-FROG traces in Figs. 2(b) and 7, respectively. Calculated values are derived by simulating 2nd and 3rd order autocorrelation traces with the power spectra from Fig. 6 and adding a residual 3rd order dispersion (TOD) to match experimental traces. The optimal TOD was 30 000 fs^3 for both configurations.

	Second		Third	
	Calc. (fs)	Measured[a] (fs)	Calc. (fs)	Measured[a] (fs)
NC	68	68	57	60
BC	56	56	48	44

[a]The uncertainty is ±2 fs for all the measured time lengths.

B. Two-color two-dimensional electronic spectroscopy (2C-2D-ES)

In a standard PE experiment, all the pulses are spectrally identical and the FWM signal is dominated by degenerate or nearly degenerate processes (diagonal terms), making the contribution of events in which the third interaction takes place at a significantly different frequency (off-diagonal terms) from the first two quite small.[38] In a 2C-2D-ES experiment, the excitation pulses (here α and β) and the probe pulse (γ) and the LO are spectrally shifted to be selectively resonant with different transitions of the system under investigation. A two-color setup can project out better non-degenerate or off-diagonal contributions, facilitating the study of energy or coherence transfer between electronic transitions.[39,40] Such an experiment can be easily implemented in our pulse-shaping assisted setup by a tailored suppression of spectral components. Fig. 8 shows an example of shaped pulses suitable for a two-color photon echo experiment, realized by applying two different TFs to the excitation and probe pulse pairs. Basically, the SLM works as a high- and a low-pass filter for the pulses α, β and γ, LO, respectively, with the cutoff wavelength at 804 nm. Equations (9) and (10) are the TFs used for the modulation of excitation pulse pair and the probe and LO pulses, respectively, with $\Delta\omega$ being the frequency FWHM

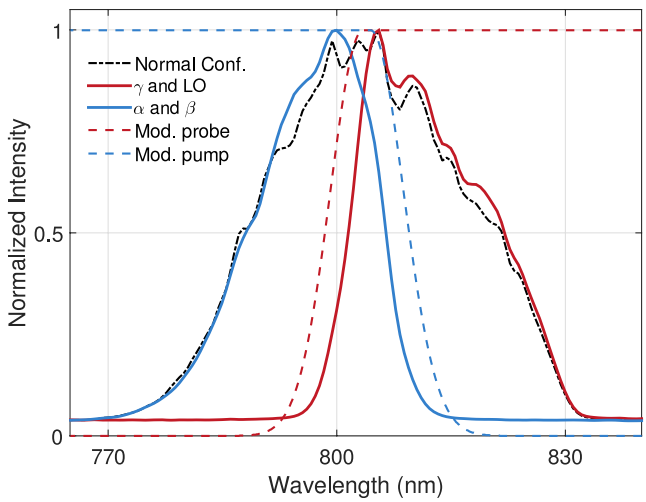

FIG. 8. Shaped pulses for two color 2D electronic spectroscopy. The TFs yielding the pulses α and β (blue solid curve) and γ and LO pulses (red solid curve) are plotted in blue and red dashed curves, respectively. The original spectrum is also depicted (black dashed-dotted curve).

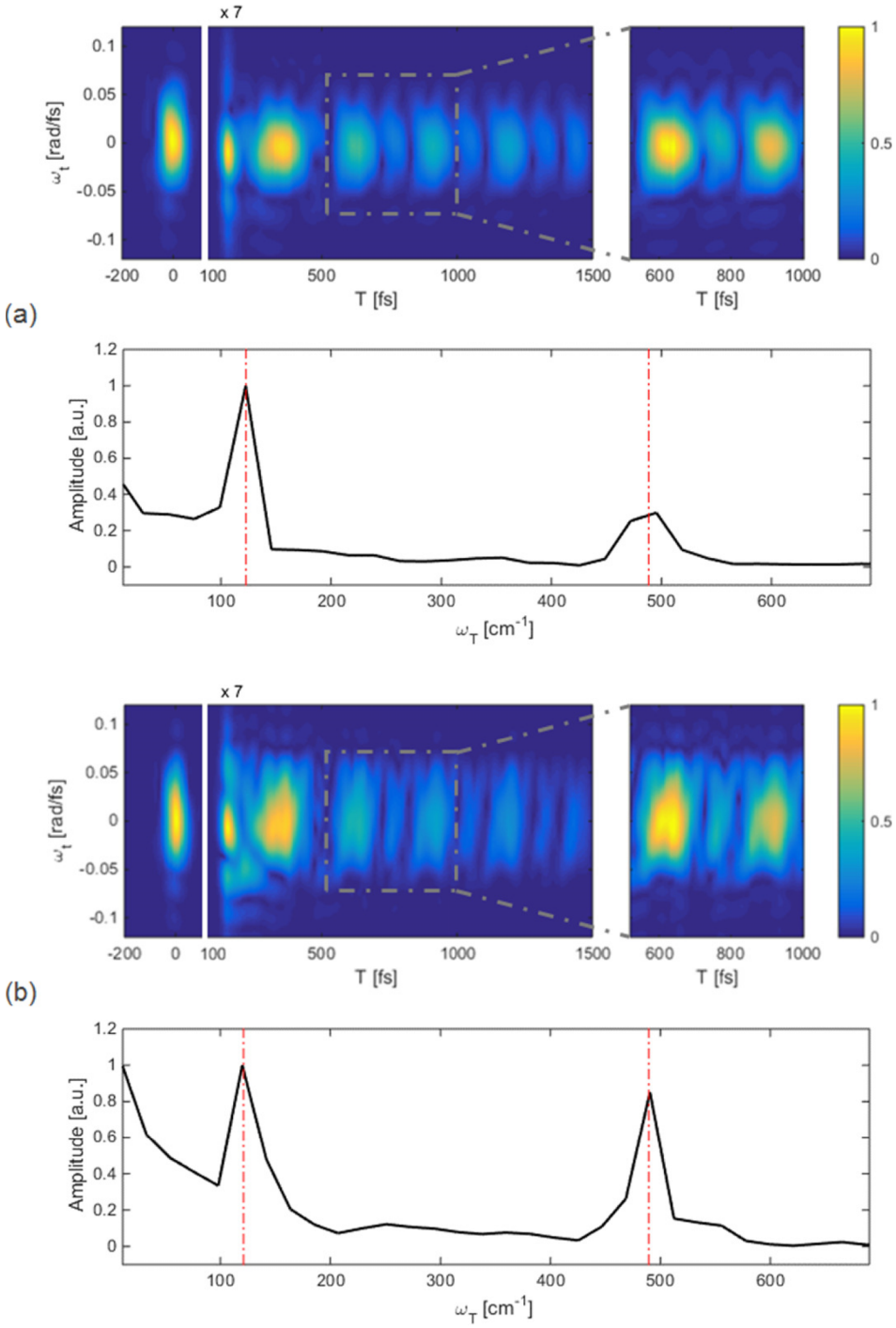

FIG. 9. Heterodyne detected transient grating experiments on pure diiodomethane with (a) normal and (b) ETR pulse configurations. The color plots show the power spectrum of the heterodyned detected signal as a function of population times. The first 100 fs are dominated by the non-resonant response of the solvent. For sake of clarity, the signal at $T > 100$ fs is multiplied by 7. The data point a clear oscillatory pattern due to the two active Raman modes (68.3 fs and 271 fs periods, see text for details) observed. The right insets show a detailed view of the temporal features due to two vibrational components. In case of the ETR configuration, the measured spectrum is broader and the temporal features are better resolved than for the normal pulse configuration, and this can also be noted in a shorter non-resonant response. This is better emphasized by the comparison of the vibrational spectra derived by Fourier transformation from the integrated signals (second and fourth panels). The increase of a baseline and of the DC component in the last panel is due to the decrease of the pulse amplitude and consequently of the FWM signal caused by the amplitude shaping (see Fig. 6 and related discussion).

of the half Gaussian-like shape of the modulation, determining level of the smoothness at the cutoff frequency, which is given by the value of ω_0,

$$M_{\alpha,\beta}(\omega) = \begin{cases} \exp\left[-(\omega-\omega_0)^2 4\ln 2/\Delta\omega^2\right], & \text{for } \omega \leqslant \omega_0 \\ 1, & \text{otherwise} \end{cases}, \tag{9}$$

$$M_{\gamma,LO}(\omega) = \begin{cases} \exp\left[-(\omega-\omega_0)^2 4\ln 2/\Delta\omega^2\right], & \text{for } \omega \geqslant \omega_0 \\ 1, & \text{otherwise} \end{cases}. \tag{10}$$

Again, both TFs are purely real to keep the pulses compressed at the sample position. Fluences at the sample position are roughly 1/3 when compared to values for normal FL pulses. This pulse scheme is suitable to investigate energy or coherence transfer processes accompanied by an energy loss or when the excited transitions undergo an energy relaxation upon excitation.

C. Phase shaping

The two previous examples are based on the modulation of the amplitude of the incoming field ($E_0(\omega)$) but shaping schemes where the phase is modulated can be of course conceived and easily implemented.[41] Indeed, any change in the phase of the three pulses will be transferred to the absolute phase of the signal by the aforesaid relation $\phi_{0,s}$

$= -\phi_{0,\alpha} + \phi_{0,\beta} + \phi_{0,\gamma}$. This paves the way to detection schemes where a spectral contribution to the signal can be suppressed or enhanced in a very similar way as in case of background suppression by phase cycling. Validation of such detection schemes is in progress.

IV. RESULTS

A. Transient grating measurements on diiodomethane

In order to provide a comprehensive and thorough validation of the experimental setup, it is mandatory to carry out measurements on well known molecular systems, so that the robustness and versatility can be tested along with the shaping methods used, which were described in Secs. III A and III B. These methods are intended in principle to serve as an experimental tool for improving the level of information on the nonlinear molecular responses. For this purpose, we first performed as a proof of principle experiment for the ETR concept, namely, a TG measurement on liquid diiodomethane (CH_2I_2) in the so-called normal configuration (i.e., only with $M_{FL}(\omega)$ applied to the modulator) and compared with known results.[14] In a second instance, the TG measurement was repeated in the ETR configuration, as shown in Eq. (8), which should—as discussed before—produce an intrinsic improvement in the time resolution of the system.

In a TG experiment, the first two pulses (α, β) coincident in time ($\tau = 0$) and produce a spatially varying index of refraction, from which the third pulse (γ) at a later time T is diffracted. There is no electronic resonance within our laser bandwidth around 805 nm. However, diiodomethane possesses different vibrational modes which are Raman active. Within the available laser bandwidth, two different modes can be addressed through impulsive stimulated Raman scattering:[14,42,43] the C–I symmetric stretch at 488 cm^{-1} (68.3 fs period) and an I–C–I bending mode at 123 cm^{-1} (271 fs period). The non-resonant TG signals for a 0.5 mm path length cuvette at room temperature are shown in Fig. 9 as the absolute recovered spectral field $|E(\omega_t,T)| = |E_s(\omega_t,T)E^*_{LO}(\omega_t,T)|$ and the experimental trace of its Fourier transform along T: $|E(\omega_t = 0.04\,\text{rad/fs}, \omega_T)|$, with the indicated vibrational frequencies in red, consisting of both slow and fast oscillatory modes. In upper case (a), no additional shaping was implemented, and the measurements were done with Fourier limited pulses (normal configuration). It can be seen that the two Raman modes can be properly resolved, being in agreement with the expected values. A zoom into the temporal response was made for the interval T (520 fs, 1 ps) to have a better resolution of the temporal features of the two vibrational components. In lower case (b), the TG signal is shown for the broad configuration. It can be noted that the temporal features are much better resolved when compared with the previous ones, accounting thus for a better experimental time resolution. This enhancement in the instrumental response function, overcoming the intrinsic temporal resolution of the original laser source and improving the quality of the measurements, corroborates the versatility and applicability of pulse shaping techniques. The fast Raman mode at 488 cm^{-1} for the lower plot in Fig. 9 is clearly of higher amplitude than in the normal configuration.

B. Photon echo measurements on IR-144 in methanol

To prove the capability of our setup to track relaxation dynamics in molecular system, we carried out 2D-ES experiments on IR-144 in methanol. We chose this molecule because it was extensively studied by Jonas and co-workers with 2D-ES and PEPS techniques.[15,16] In addition, its absorption and emission spectra are spectrally well separated, with the absorption and the emission located at $\lambda < 800$ nm and >800 nm, respectively (see Fig. 10).

Rephasing and non-rephasing measurements were first done on the dye IR-144 in normal configuration and compared with the literature. The PEPS signals were calculated from the 2D measurements by integrating the absolute value of the signal field along the detection time. Then, a two-color 2D-ES experiment was carried out under identical conditions in order to enhance the PE peak-shift by selectively choosing the adequate pump and probe frequencies in the pulse sequence interaction.

The experimental results in standard configuration are reported in Fig. 11. To follow the early solvation dynamics of the dye due to solvent relaxation (fast components of the methanol solvation response function: 30 fs and 280 fs), PE measurements are performed for five different population times T. The heterodyned experimental results show a clear change in amplitude and phase between $T = 0$ and $T = 200$ fs. In particular, the transformation from an asymmetric shape with a structured phase to a round peak with a constant phase definitively speaks for a decoherence mechanism. The PEPS for the different population times T (Fig. 12(a)) confirms this picture. More important for the present discussion is that these results are in good agreement with measurements from the literature.[15,16] The red shift of the PE signal along ω_t in Fig. 11 nicely confirms that the dominant contribution to the relaxation dynamics originates from a dynamical Stokes shift of the excited molecules. This result fully agrees with the observed PEPS decay and with previous work.[15,16] It also suggests that the implementation of a 2C-2D-ES shows promise to be more sensitive to excited state signals and could provide a better signal and more details on excited state dynamics.

Thus, to give another example of the advantages arising from the versatility of a pulse shaper based setup, we conducted a 2C-2D-ES experiment on the same molecules and with the same experimental conditions where the excitation and probe pulses were optimized to be more resonant with the

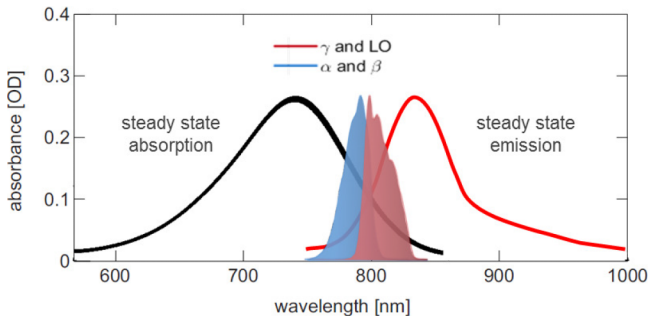

FIG. 10. Steady-state absorption and emission spectra of IR-144 in methanol. The spectral intervals covered by the excitation and probe pulse pairs are also marked.

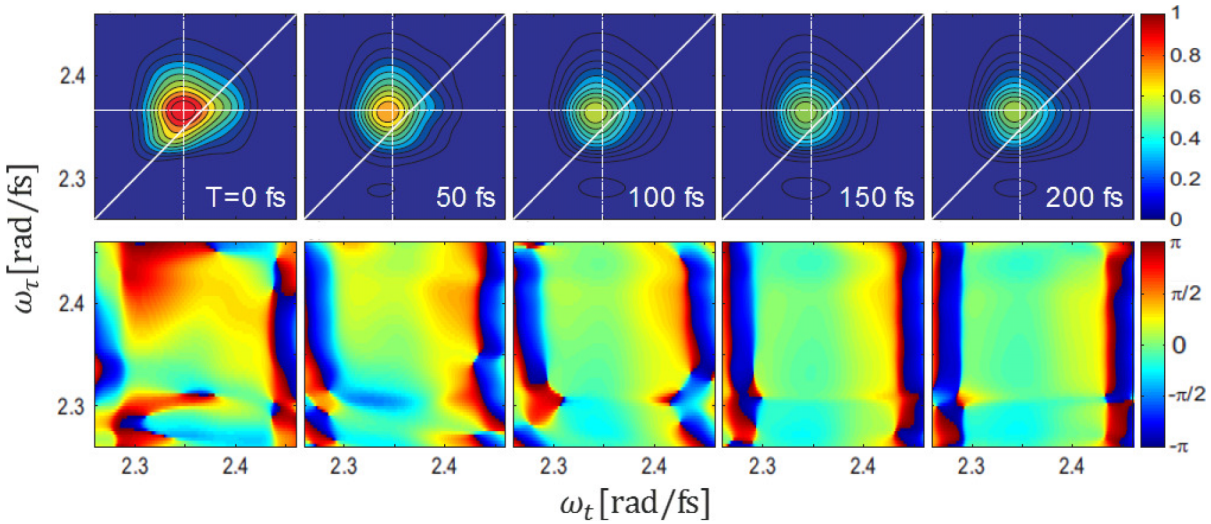

FIG. 11. Heterodyned photon echo signal for five different population times on IR-144 in methanol. Absolute value (top row) and spectral phase (bottom row) of the signal in frequency-frequency domain (2D-ES spectrum). The experiment is performed with approximately 14 nJ/pulse at the sample position. By amplitude modulation, the intensity of the local oscillator was adjusted to be approximately ten times larger than the PE signal at $T = \tau = 0$. The signal was integrated over 10 000 shots (40 ms) and the solution was flowed through a 0.2 mm path length cell.

absorption and emission bands, respectively. This condition was achieved by setting a cutoff wavelength at 804 nm for the long and short pass filters for the excitation and probe and LO TFs, respectively (see Figs. 10 and 12). As expected, increasing the contribution to the signal generated by excited molecules makes the previously observed dynamics more evident and pronounced, as clearly proved by the comparisons of the two PEPS scans. In Fig. 12, we observe indeed that (i) the extent of the peak shift at time zero is more pronounced when we selectively detect signals from excited molecules, and (ii) in contrast to the standard configuration, we can still observe a non-zero peak shift value after 200 fs. The latter indicates an enhanced sensitivity rather than a change in the decoherence time since in both cases, the PEPS disappears or almost disappears in the same time scale. This is a clear evidence of the validity of linear response approximation for IR-144 in methanol, namely, that the solvent-solute coupling and the local solvation dynamics are unaffected by the specific electronic state of the molecular probe.[21] Concerning the increase of the peak shift at time zero, its extent is due to a competition between the homogeneous dephasing and the inhomogeneous rephasing. Since a comparable decoherence time was measured, these results point to a better rephasing ability of the system and to a greater inhomogeneity of the energy gap transition frequency of the excited state molecule with respect to the ones in the ground state. This result sounds reasonable assuming that an excited molecule is expected to be more polarizable or polar and therefore more affected by solvent inhomogeneities. Remarkably, the energy gap loss triggered by the new solute electronic configuration (the dynamical Stokes shift from the absorption Frank-Condon region) is not accompanied by a loss in the memory stored in the just-excited molecular

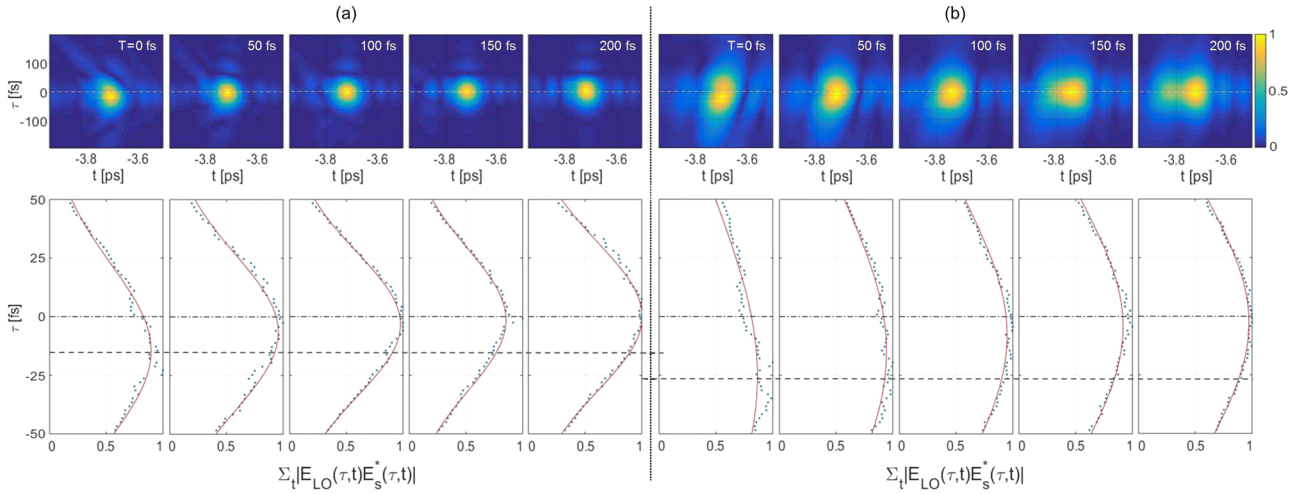

FIG. 12. (Top row) Photon echo signal on the dye IR-144 in methanol in the $\tau - t$ domain (see caption of Fig. 11 for experimental conditions) around the LO time delay for five different population times T. (Bottom row) The respective absolute values integrated along t, the so-called three pulse PEPS. (a) Measurements with Fourier-transform limited pulses (normal configuration) and no additional shaping implemented. (b) Two-color measurements (see Fig. 10). The $\tau = 0$ fs and the time zero peak shift (the τ of the maximum) in the two cases are marked (dashed-dotted and dashed lines, respectively). An enhancement of the time-zero peak shift is observed in the two-color experiment compared to the normal configuration.

ensemble. This is a tentative explanation which deserves more experimental and theoretical evidence, but for the aim of the present article, it clearly indicates the improved insightfulness of a 2C-2D-ES experiment and its unique advantages when compared to a conventional experiment.

V. CONCLUSIONS

In this contribution, we report on our recently implemented non-collinear 2D-FWM spectrograph based on fully computer-controlled shaping of all interacting beams and the local oscillator. It is based on a 2D liquid crystal spatial light modulator and allows for high fidelity automated 2D phase and amplitude shaping of several non-collinear, phase-coherent pulses. This offers the unique capability to have independent control on wavevectors, pulse timings, and phases, as well as spectral content of each field. This approach can generate waveforms of high complexity, such as multiple pulses[41] or chirped pulses, with a superior flexibility when compared with conventional FWM setups. For instance, time scans over several picoseconds with an absolute time resolution of 150 as are achieved, without mechanical parts. More important, all pulses are outstandingly phase stable (the present scheme could be used even for experiments in the deep UV, with a suitable SLM[44]). This scheme was initially conceived to investigate multi-excitons in semiconductor quantum wells[45] and we successfully validate it as a valuable tool for electronic spectroscopy on molecular systems in the liquid phase. Moreover, it allows to achieve the best pulse compression at the sample position and a smart background suppression with no extra noise added to the signal and no detriment of the experiment duration and acquisition duty cycle. We recently started to explore the peculiar flexibility of this nonstandard approach to develop novel detection schemes and measuring methodologies, unfeasible with conventional setups. Here, we reported two illustrating cases: (i) boosting the time-resolution and the detected spectral range; (ii) the enhancement of signals from specific molecular states and energy transfer processes by optimal tuning of the excitation and probe pulses. As briefly commented, detection schemes based on phase modulation can be easily implemented with such pulse-shaped assisted setups. In such schemes, specific signals are suppressed or enhanced by pure destructive/constructive interferences between the signal and the LO. In contrast to pure amplitude modulation, the selectivity is not achieved by tailoring the spectral distribution of the excited molecule but by a selective detection of the emitted signals. We are currently further developing this nonstandard approach and verifying its potential. The versatility of such implementation paves the way to design even more sophisticated nonstandard schemes based on simultaneous phase and amplitude modulation, tailored to specific physical system or physico-chemical processes of interest.

ACKNOWLEDGMENTS

Financial support by European Union (ERC Starting Grant No. 279599) and the Swiss NSF through the NCCR MUST is gratefully acknowledged.

[1]A. M. Weiner, Rev. Sci. Instrum. **71**, 1929 (2000).
[2]Y. Silberberg, Annu. Rev. Phys. Chem. **60**, 277 (2009).
[3]N. Dudovich, D. Oron, and Y. Silberberg, Nature **418**, 512 (2002).
[4]H. Kawashima, M. M. Wefers, and K. A. Nelson, Annu. Rev. Phys. Chem. **46**, 627 (1995).
[5]Y.-C. Cheng and G. R. Fleming, Annu. Rev. Phys. Chem. **60**, 241 (2009).
[6]S.-H. Shim and M. T. Zanni, PCCP **11**, 748 (2009).
[7]V. Prokhorenko, A. Halpin, and R. Miller, Opt. Express **17**, 9764 (2009).
[8]P. Tian, D. Keusters, Y. Suzaki, and W. S. Warren, Science **300**, 1553 (2003).
[9]T. Hornung, J. C. Vaughan, T. Feurer, and K. A. Nelson, Opt. Lett. **29**, 2052 (2004).
[10]J. C. Vaughan, T. Hornung, T. Feurer, and K. A. Nelson, Opt. Lett. **30**, 323 (2005).
[11]K. Gundogdu, K. W. Stone, D. B. Turner, and K. A. Nelson, Chem. Phys. **341**, 89 (2007).
[12]D. Turner, K. W. Stone, K. Gundogdu, and K. A. Nelson, Rev. Sci. Instrum. **82**, 081301 (2011).
[13]A. Rondi, Y. Rodriguez, T. Feurer, and A. Cannizzo, Acc. Chem. Res. **48**, 1432 (2015).
[14]J. C. Vaughan, T. Hornung, K. W. Stone, and K. A. Nelson, J. Phys. Chem. A **111**, 4873 (2007).
[15]J. D. Hybl, Y. Christophe, and D. M. Jonas, Chem. Phys. **266**, 295 (2001).
[16]D. M. Jonas, Annu. Rev. Phys. Chem. **54**, 425 (2003).
[17]A. Konar, J. D. Shah, V. V. Lozovoy, and M. Dantus, J. Phys. Chem. Lett. **3**, 1329 (2012).
[18]A. Konar, V. V. Lozovoy, and M. Dantus, J. Phys. Chem. Lett. **3**, 2458 (2012).
[19]Y. Nagasawa, J. Photochem. Photobiol., C **12**, 31 (2011).
[20]F. Frei, A. Galler, and T. Feurer, J. Chem. Phys. **130**, 034302 (2009).
[21]S. S. Mukamel, *Principles of Nonlinear Optical Spectroscopy* (Oxford University Press, New York, 1995).
[22]F. Milota, J. Sperling, A. Nemeth, D. Abramavicius, S. Mukamel, and H. F. Kauffmann, J. Chem. Phys. **131**, 054510 (2009).
[23]M. H. J. Oh, M. R. Salvador, C. Y. Wong, and G. D. Scholes, ChemPhysChem **12**, 88 (2011).
[24]M. D. Fayer, Annu. Rev. Phys. Chem. **60**, 21 (2009).
[25]P. Hamm, J. Helbing, and J. Bredenbeck, Annu. Rev. Phys. Chem. **59**, 291 (2008).
[26]G. Scholes, G. Fleming, A. Olaya-Castro, and R. van Grondelle, Nat. Chem. **3**, 763 (2011).
[27]A. Halpin, P. J. M. Johnson, R. Tempelaar, R. S. Murphy, J. Knoester, T. L. C. Jansen, and R. J. D. Miller, Nat. Chem. **6**, 196 (2014).
[28]M. L. Cowan, J. P. Ogilvie, and R. J. D. Miller, Chem. Phys. Lett. **386**, 184 (2004).
[29]T. Brixner, T. Mancal, I. V. Stiopkin, and G. R. Fleming, J. Chem. Phys. **121**, 4221 (2004).
[30]T. Brixner, J. Stenger, H. M. Vaswani, M. Cho, R. E. Blankenship, and G. R. Fleming, Nature **434**, 625 (2005).
[31]U. Selig, F. Langhojer, F. Dimler, T. Löhrig, C. Schwarz, B. Gieseking, and T. Brixner, Opt. Lett. **33**, 2851 (2008).
[32]U. Selig, C.-F. Schleussner, M. Foerster, F. Langhojer, P. Nuernberger, and T. Brixner, Opt. Lett. **35**, 4178 (2010).
[33]B. A. West and A. M. Moran, J. Phys. Chem. Lett. **3**, 2575 (2012).
[34]C.-H. Tseng, S. Matsika, and T. C. Weinacht, Opt. Express **17**, 18788 (2009).
[35]M. Bradler, P. Baum, and E. Riedle, Appl. Phys. B **97**, 561 (2009).
[36]N. Krebs, I. Pugliesi, J. Hauer, and E. Riedle, New J. Phys. **15**, 085016 (2013).
[37]G. Cerullo and S. De Silvestri, Rev. Sci. Instrum. **74**, 1 (2003).
[38]R. Agarwal, B. S. Prall, A. H. Rizvi, M. Yang, and G. R. Fleming, J. Chem. Phys. **116**, 6243 (2002).
[39]J. M. Dawlaty, D. I. G. Bennett, V. M. Huxter, and G. R. Fleming, J. Chem. Phys. **135**, 044201 (2011).
[40]J. A. Myers, K. L. Lewis, P. F. Tekavec, and J. P. Ogilvie, Opt. Express **16**, 17420 (2008).
[41]P. Wen and K. A. Nelson, J. Phys. Chem. A **117**, 6380 (2013).
[42]Y.-X. Yan and K. A. Nelson, J. Chem. Phys. **87**, 6240 (1987).
[43]K. A. Nelson and E. Ippen, in *Advances in Chemical Physics* (John Wiley & Sons, Inc., Hoboken, NJ, USA, 1989), Vol. 75.
[44]T. Tanigawa, Y. Sakakibara, S. Fang, T. Sekikawa, and M. Yamashita, Opt. Lett. **34**, 1696 (2009).
[45]K. W. Stone, K. Gundogdu, D. B. Turner, X. Li, S. T. Cundiff, and K. A. Nelson, Science **324**, 1169 (2009).